ARTICLE

Label-Free Imaging of Single Microtubule Dynamics Using Spatial Light Interference Microscopy

Mikhail E. Kandel,[†] Kai Wen Teng,[‡,§] Paul R. Selvin,[‡,§,∥] and Gabriel Popescu[*,†,⊥]

[†]Quantitative Light Imaging Laboratory, Department of Electrical and Computer Engineering, Beckman Institute of Advanced Science and Technology, [‡]Center for the Physics of Living Cells, [§]Center for Biophysics and Quantitative Biology, [∥]Department of Physics, and [⊥]Department of Bioengineering, University of Illinois, Urbana, Illinois 61801, United States

S *Supporting Information*

ABSTRACT: Due to their diameter, of only 24 nm, single microtubules are extremely challenging to image without the use of extrinsic contrast agents. As a result, fluorescence tagging is the common method to visualize their motility. However, such investigation is limited by photobleaching and phototoxicity. We experimentally demonstrate the capability of combining label-free spatial light interference microscopy (SLIM) with numerical processing for imaging single microtubules in a gliding assay. SLIM combines four

different intensity images to obtain the optical path length map associated with the sample. Because of the use of broadband fields, the sensitivity to path length is better than 1 nm without (temporal) averaging and better than 0.1 nm upon averaging. Our results indicate that SLIM can image the dynamics of microtubules in a full field of view, of 200×200 μm^2, over many hours. Modeling the microtubule transport *via* the diffusion-advection equation, we found that the dispersion relation yields the standard deviation of the velocity distribution, without the need for tracking individual tubes. Interestingly, during a 2 h window, the microtubules begin to decelerate, at 100 pm/s^2 over a 20 min period. Thus, SLIM is likely to serve as a useful tool for understanding molecular motor activity, especially over large time scales, where fluorescence methods are of limited utility.

KEYWORDS: *microscopy, microtubules, cellular cytoskeleton, label-free, quantitative phase imaging, high-sensitivity detection, single particle imaging*
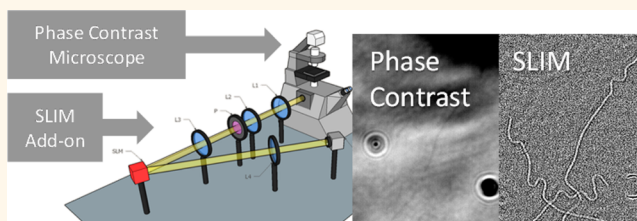
INTRODUCTION

Microtubules are elements of the cytoskeleton with very interesting, incompletely understood dynamic properties.[1−9] Beside their structural role in the cell, microtubules also act as roadways for molecular motor-mediated intracellular traffic[10,11] and play a crucial role in chromosome segregation during mitosis.[12,13] Due to their ubiquitous role in the cellular cytoskeleton, microtubule malfunction has been associated with various illnesses, from cancer[14] to Alzheimer's disease.[15] Studying dynamic single microtubules is challenging due to their minute tubular structure, 24 nm outer diameter, 12 nm inner diameter, with lengths of up to tens of microns.[16] Most commonly, they are visualized using immunofluorescence.[17] Fluorescence techniques have enabled a number of break-through discoveries related to the nanoscale dynamics of microtubules and their associated molecular motors.[18−23] In particular, fluorescence speckle microscopy has been employed successfully to study tubulin dynamics.[24,25] Still, fluorescence imaging continues to be limited by phototoxicity,[26] which affects cell function, and photobleaching,[27] which narrows

down the window for continuous imaging to several minutes. In this context, fluorescence-free imaging methods have been developed in parallel for studying microtubules. For example, early on, Inoue *et al.* developed a polarization-based method to image the mitotic spindles of large cells,[28] and Svoboda *et al.* used optical tweezers to discover kinesin's moving steps.[29] These methods demonstrated that scattering contrast can provide sufficient sensitivity for studying single microtubules, without the drawbacks due to fluorescence. However, they are not without limitations: birefringence-based measurements require polarization optics, are extremely sensitive to alignment, and do not always yield the required sensitivity for single microtubule imaging; optical tweezers typically rely on high optical power, which may result in thermal artifacts and the need for a micron-sized probe. More recently, Andrecka *et al.* have used an interferometric scattering technique to image

microtubule transport.[30] Such interferometric scattering systems,[31] reminiscent of reflection interference contrast microscopy, rely on the interference[32] between the waves scattered by the structure of interest and those reflected by the substrate. As a result, the interference detected lacks control over the amplitude and phase of the two interfering fields, which essentially results in low fringe visibility and, thus, a low signal-to-noise ratio.

In response to these challenges, we propose a different approach that allows for single microtubule imaging, without labels, over arbitrary time scales. Importantly, our method is "full-field" and, thus, yields nanoscale-sensitivity imaging over extremely large fields of view, $200 \times 200 \ \mu m^2$ on our camera, which is orders of magnitude larger than what can be achieved *via* scattering reflection measurements. Our method relies on spatial light interference microscopy (SLIM),[33−35] which is a highly sensitive form of quantitative phase imaging,[36] and time-axis numerical processing to significantly increase signal-to-noise. In essence, SLIM combines phase contrast microscopy with holography,[37] to yield optical path length (or delay) maps associated with light transmitted through transparent structures. The signals are very sensitive to the object structure, down to the subnanometer scale. SLIM is capable of an acquisition rate of up to 16 four-megapixel phase images per second. We apply SLIM to continuous quantitative data in gliding assay experiments over time scales from milliseconds to days, which is impossible to achieve using fluorescent techniques. Because the microtubule images are quantitative, meaning that the signal values are constant throughout the experiment, we show that the time-lapse data can be translated into dynamic light scattering results.

We measured the dispersion relation associated with the spatiotemporal fluctuations due to microtubule gliding, *i.e.*, the temporal bandwidth *vs* spatial frequency. Our results indicate that the dispersion relation is consistent with deterministic, active transport. The values for the standard deviation of the velocity were extracted quantitatively, and the results matched well those obtained by manually tracking each microtubule. We observed that, by monitoring microtubule transport continuously over long durations, it is possible to recover a constant deceleration of $100 \ pm/s^2$ over more than 20 min. This dispersion-relation phase spectroscopy (DPS) approach is an efficient means to study microtubule transport, as it provides robust information about the velocity distribution, intrinsically averaged over the ensemble of tubes within the field of view.

RESULTS AND DISCUSSION

Our imaging system (Cell Vista SLIM Pro, Phi Optics, Inc.) is depicted in Figure 1a and described in more detail elsewhere (see refs 35 and 38 and Methods). Briefly, SLIM is implemented as an add-on upgrade unit to an existing phase contrast microscope. The idea is to turn the phase contrast ring of the microscope objective into a tunable phase shifter, such that the phase between the incident and scattered light can be controlled. While in phase contrast the phase shift introduced by the ring is fixed at $\pi/2$, in SLIM, we acquire four intensity images, corresponding to the 0, $\pi/2$, π, and $3\pi/2$ phase shifts. As a result, the amplitudes of the scattered and incident light are decoupled, and the phase shift map due to the microtubules is retrieved (see Methods).

We applied SLIM to image single microtubules in gliding assays,[39] which are a valuable tools for studying molecular motor activity in a highly controlled manner. The microtubule
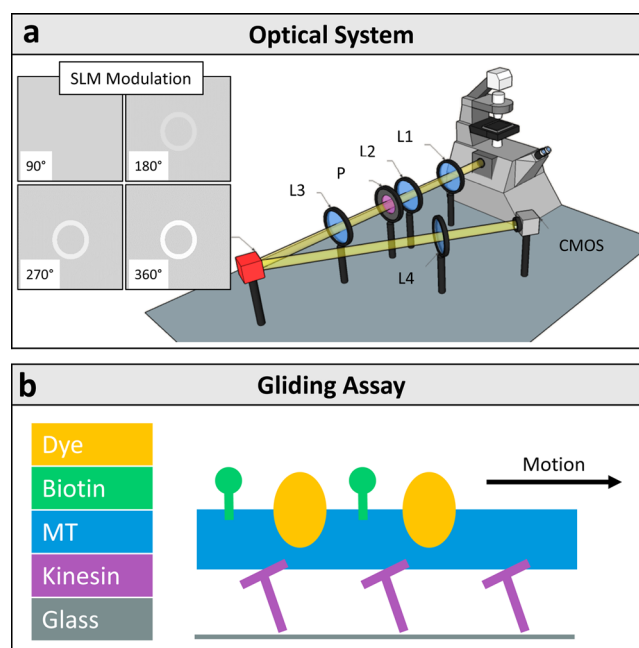

Figure 1. The optical system and assay. (a) In SLIM, the phase shift between transmitted and scattered light is modulated with a phase mask externally matched to the conjugate plane of the objective (red component). The setup is attached to the output port of a conventional microscope. (b) In a typical gliding assay, microtubules (MTs) are pushed by surface attached motor proteins. The gliding velocity of the microtubules provides a measure of the protein's motility. See Methods for a detailed description of the components, along with the gliding assay protocol.

gliding assay reveals how efficiently different motors work together,[40] as well as the effect of various microtubule binding drugs and post-translational modification on the gliding velocity of kinesin.[39,41]

Figure 1b illustrates how the microtubule slides on a substrate covered with kinesin molecules (see Methods for details on sample preparation). We imaged microtubules, with and without biotin labels, gliding on kinesin for 320 s, at an acquisition speed of 6.5 frames/s, and repeated the experiments 3 times. Due to the large field of view, many individual tubulin structures can be monitored at the same time. We note that our system is capable of acquiring a maximum of 16 SLIM images per second. However, to increase signal-to-noise, we chose a lower rate of 6.5 frames/s.

Remarkably, the phase shift associated with a single microtubule is of the order of 1 mrad, which yields a refractive index of 1.475 (see Methods for the scattering calculations based on the first Born approximation). Such small phase values are measurable in SLIM because of the white light illumination, which averages out the speckles in the background and, thus, yields very high spatial sensitivity. Figure 2a−d underscores the improvement that SLIM brings over a typical phase contrast image. Because each SLIM image is the result of combining 4 intensity frames, much of the background noise, due to, for example, residues and substrate imperfections, is subtracted out very effectively. Specifically, the amplitude modulation in the phase contrast image (Figure 2a) is largely removed in the SLIM image (Figure 2b, d). Simply put, incoherent contributions to the imaging field are insensitive to phase-shifting and are not registered in the interferometric image. The maximum SLIM frame rate is limited by the liquid
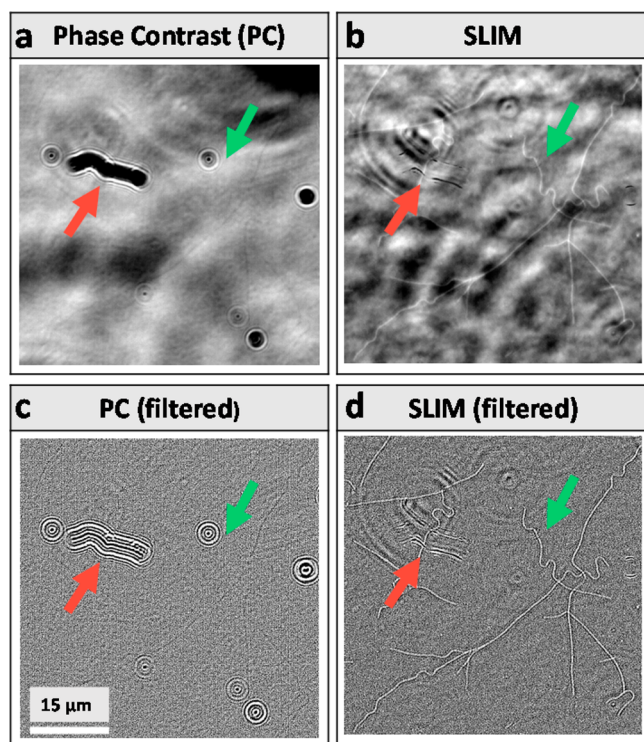
Figure 2. SLIM enhances phase contrast microscopy. (a) Phase contrast frame used in the SLIM interferometric reconstruction process. (b) By eliminating the light outside of the coherence gate, the SLIM system performs implicit background subtraction. The amplitude modulation pointed by the red arrow in (a) completely disappears in (b). Further, phase objects that are submerged under an incoherent background such as the single microtubule (green arrow) become clearly visible. (c, d) Images shown in (a) and (b) are spatial high-pass filtered and temporal averaged (see Methods for details of the procedure).

crystal modulator to approximately 15 frames/s, corresponding to a 60 Hz frame refresh rate.

It is the pure phase information, proportional to the refractive index of the structure, that allows us to image microtubules indefinitely, from milliseconds to hours. This particular advantage is illustrated in Figure 3, where we compare fluorescence and SLIM imaging of the same microtubules. Note that SLIM perfectly overlays with the fluorescence channels of the microscope such that we can easily image the same structure with both modalities. To minimize photobleaching, the fluorescence shutter was closed between frames. Nevertheless, after 3 min of imaging, the fluorescence signal photobleached, and the image faded away. On the other hand, using SLIM, we imaged continuously the same microtubules over the entire period, without a decrease in contrast.

In order to demonstrate the ability of SLIM data to provide quantitative information about the microtubule motility, we manually tracked a large number of them, both tagged with biotin and untagged. We computed a number of parameters that characterize the motility: speed, direction of motion, and distribution of velocity. Figure 4 summarizes these results. First, we found that the velocity distributions agree with previous reports (see, *e.g.*, ref 42). Furthermore, we found that the lower microtubule speeds were associated with "curvier" trajectories, as defined by the variance of the direction of the velocity. It is rather interesting that the mean-speed to mean-angle change ratio is approximately constant. This is consistent with a constant momentum transfer in the transverse direction from the substrate to the microtubule, as follows. Consider the inset of Figure 4f, indicating the momentum conservation during an event that causes a direction change. This change in angle is due to a transverse momentum contribution due to the molecular motors, $\mathbf{p}$. Assuming that during this interaction, the initial velocity, $\mathbf{v}_1$, and final velocity, $\mathbf{v}_2$, are different in only
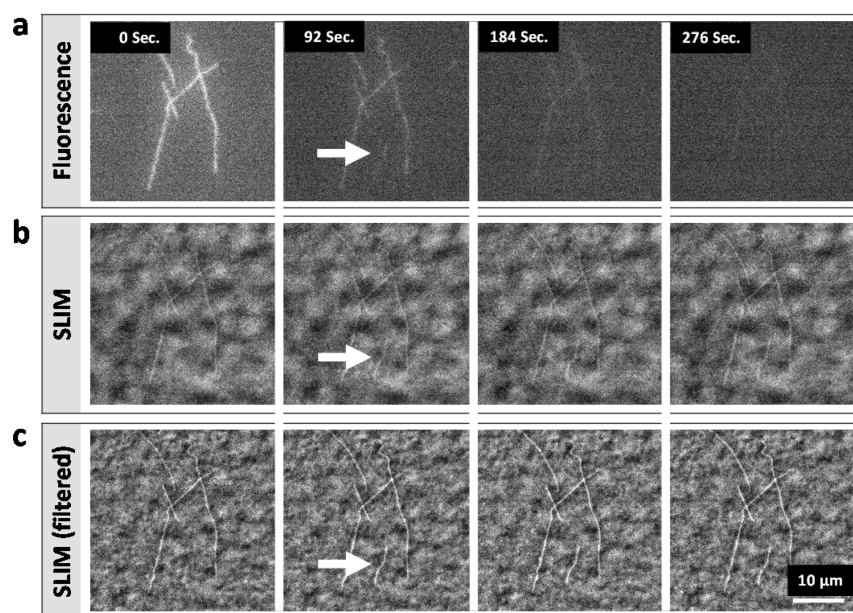

Figure 3. SLIM enables continuous observation without photobleaching. (a) Fluorescence microscopy image, using the HiLyte 488 dye. Note that a descending microtubule is not visible due to photobleaching (arrow). (b) SLIM images of the same field of view. (c) For easier visualization, the SLIM sequence was filtered with a spatial high-pass filter and with a rolling 5-tap median temporal filter (see Methods for details). This averaging scheme is implemented in real-time in our acquisition system. The corresponding videos can be found in the Supporting Information, Videos 1, 2, 3, 4, and 5.
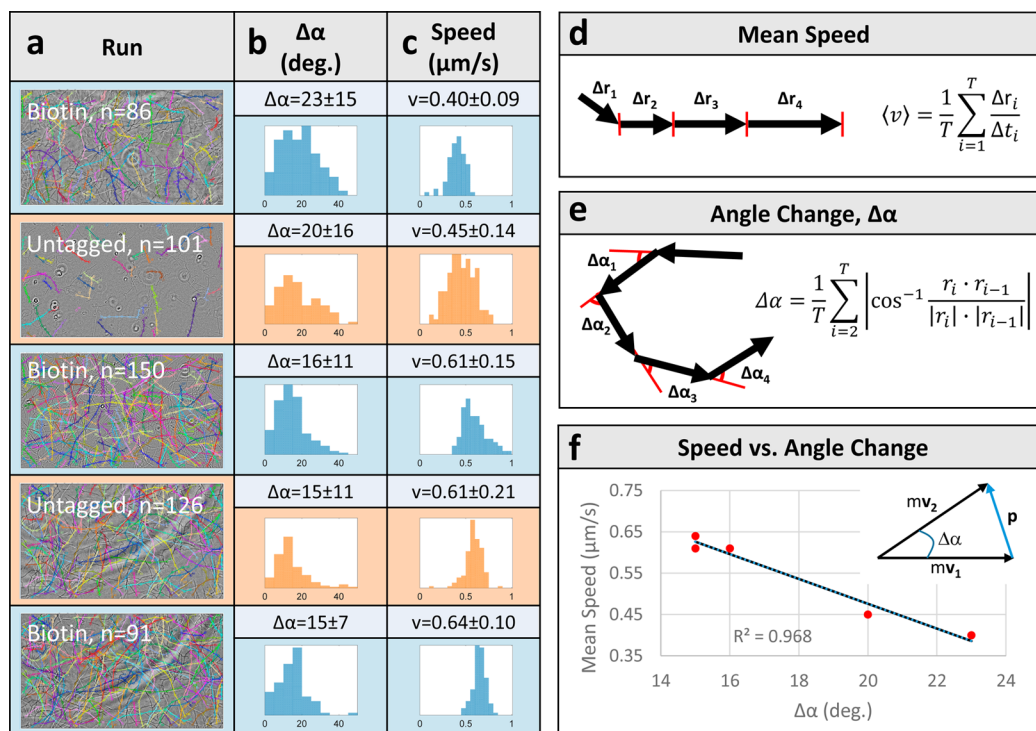
Figure 4. Single microtubule tracking analysis. (a) Representative fields of view used to track microtubules, for tagged and untagged preparations, as indicated (each field of view spans $200 \times 200 \ \mu m^2$). (b) Histogram of the angular change in direction associated with the leading end of individual microtubules; histograms correspond to the fields of view in (a). (c) Histogram of speed distributions for the different fields of view shown in (a). (d) Schematic showing the definition of the angular change represented in (b). (e) Schematic for defining the speed represented in (c). (f) Mean speed *vs* angular change. The inset shows the momentum conservation diagram for a microtubule changing direction: *m*, mass of the microtubule, v_1, initial velocity, v_2, final velocity, and p, momentum transfer from the molecular motors on the substrate.

direction and not magnitude, $|v_1| = |v_2| = v$, the conservation of momentum requires that $p = 2mv\sin(\Delta\alpha/2)$, which implies $\Delta\alpha \approx p/mv \propto 1/v$. Thus, our measurements suggest that, on average, the change in direction is consistent with a constant momentum transfer from the molecular motors in the substrate.

We next turn to the investigation of possible effects of biotin tagging on microtubule kinetics by comparing the angle change and velocities between tagged and untagged microtubules. Analyzing the angle change parameter ($\Delta\alpha$) with a Mann–Whitney U test,[43] we see that there is little difference between tagged and untagged microtubules ($p = 0.66$). At a first glance, the mean gliding velocities appear separated into two categories; motivating us to bin the experimental runs into velocities with mean $v_1 = 0.4 \ \mu m/s$ and $v_2 = 0.6 \ \mu m/s$. Using another Mann–Whitney U test, we find that for the slow category, v_1, there appears to be a velocity increase with tagging ($p = 0.0052$), while for the faster category, v_2, there appears to be a decrease ($p = 6.75 \times 10^{-8}$). We conclude that the difference between experimental runs was too significant to support a conclusion regarding the influence of tagging on microtubule motion (see Section 2 of the Supporting Information for details).

While tracking individual tubes is effective, this procedure is extremely tedious. Therefore, we tested whether DPS can be applied to such extremely weak scatterers.[44,45] DPS was developed to study intracellular mass transport and proved to be a valuable tool to distinguish between diffusive and deterministic transport.[44] The principle of DPS relies on the quantitative data provided by QPI and on modeling the

transport using a diffusion-advection equation (see SI for details) and describes transport phenomena that are subject to both diffusion and drift. The resulting dispersion relation has the form:

$$\Gamma(q) = \Delta v q + D q^2 \tag{1}$$

where Γ is the decay rate (temporal bandwidth) associated with the spatial mode q, D is the diffusion coefficient, and Δv is the width of the velocity distribution. Figure 5 shows the DPS procedure for analyzing full-field, time-lapse SLIM images of microtubules. First, we take the 2D Fourier transform of each image. From the time-lapsed spatial Fourier transform, we calculate the temporal bandwidth at each spatial frequency, q. This 2D map, $\Gamma(q)$, incorporates frequency information from the entire 3D data set. Assuming isotropy, the 2D map can be further azimuthally averaged to obtain a 1D function, $\Gamma(q)$, with $q = |\mathbf{q}|$. As shown in Figure 5, fitting the linear portion of these plots with eq 1 yields, Δv, the width of velocity distribution. We collected images over 100 min and found that, after approximately 20 min, the value of Δv considerably decreases linearly in time, most likely due to ATP depletion. This result indicates that, in time, the velocity distribution narrows down, *i.e.*, the probability of having high speeds decreases. This linear decrease with time results in a constant deceleration, computed to be approximately $a = 100 \ pm/s^2$. Note that this subtle change in velocity with time could not be easily measured with fluorescence imaging, as photobleaching sets in after 2–3 min of continuous imaging.

It is remarkable that the SLIM images can be interpreted in terms of angular scattering representation. Measuring angular
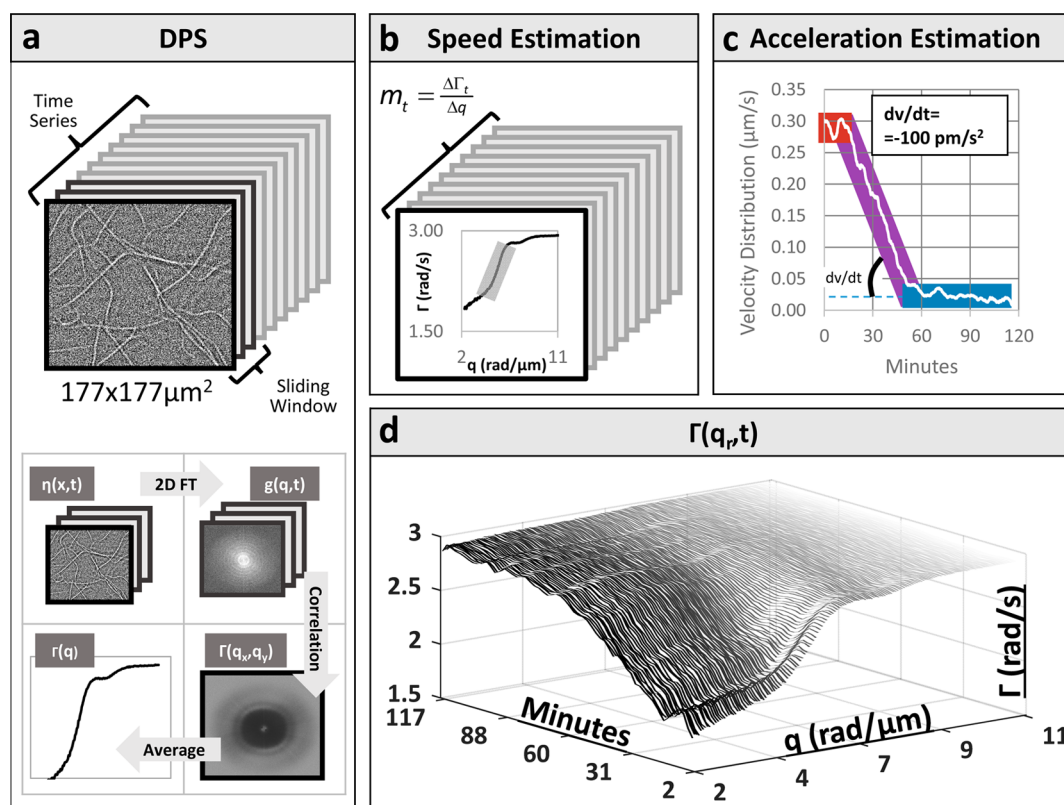
Figure 5. Long-term imaging reveals deceleration of microtubules. (a) The dispersion relation is computed over a temporal window of 128 frames for each time point in the series. In short, the method involves taking the 2D Fourier transform of each image and computing the decay (or temporal bandwidth) at each spatial frequency. After the isotropic assumption, the volumetric data are reduced to a single dimension. When the window is advanced, one of the old Fourier transforms is discarded, and the bandwidth is recomputed. (b) Microtubule gliding velocity standard deviation was calculated using DPS, on a rolling basis over approximately 15,000 frames, taken 0.475 s apart. (c) In this run, after 20 min, the spread of the velocity distribution begins to decrease, with virtually no significant motion after the 60 min mark. (d) DPS signals *vs* time shows continuous change in slope.

scattering from a 24 nm diameter tube would be extremely challenging using traditional goniometer-based systems, as in such an experiment, the power of the field scattered at each angle would be measured serially. By contrast, in SLIM, at each pixel on the detector, the fields scattered at various angles add up coherently. As a result, SLIM is a much more sensitive scattering measurement than any of the traditional methods.[46] Of course, the microtubules are pure phase objects, completely invisible to bright-field imaging systems. It is the result of the interferometric scheme and the phase retrieval process that we can detect such extremely thin objects.

Compared to fluorescence methods, SLIM is not bound by phototoxicity and, thus, can be used to imagine over virtually indefinitely long time scales. The quantitative information allows us to describe the microtubule transport *via* a diffusion-advection equation that governs the fluctuations of mass density. We found that, over a broad interval of spatial frequencies, q, the dispersion relationship that describes the motion is essentially linear: $\Gamma(q) = \Delta v q$ is consistent with the active transport expected from molecular motors. The proportionality constant Δv represents the width of the velocity distribution. Note that this analysis does not require individual tracking of the microtubules, but, rather, is an automated form of analysis that operates on the entire time-resolved image stack. As the Fourier transform needs only to be taken for new frames, the analysis is extremely fast, on the order of 400 ms for a 128 frame window, with 4 megapixels at each time point.

Imaging the gliding process over 2 h, we discovered that the velocity standard deviation decreases linearly in time. Thus, we measured microtubule deceleration using the same sample. The two motor domains of kinesin act as enzymes which produce work by spending ATP. We expect kinesin to follow Michaelis–Menten kinetics, just like any other enzymes, where the catalytic rate of kinesin (in this case velocity) increases as a function of substrate concentration (ATP).[47,48] Thus, the deceleration can be explained by ATP depletion. We anticipate that these type of data will be very informative in studying molecular motor mechanical work *vs* ATP concentration and other factors such as molecular loads (*e.g.*, fluorescent tags).

Ultimately, we aim to use SLIM for imaging microtubule kinetics in live cells. Because of the heterogeneous background introduced by the cytoplasm, we expect imaging phase shifts associated with single microtubules inside cells to be more challenging. However, using the fluorescence channel, we can locate the microtubules and optimize our data acquisition and numerical processing to extract quantitative microtubule information from live cells. These studies are the subject of current efforts.

METHODS

Spatial Light Interference Microscopy (SLIM). In s SLIM, a phase ring conjugate to the pupil plane is used to introduce sequential phase shifts between the scattered and transmitted components of the object perturbed field. Here we used a modified version of the design
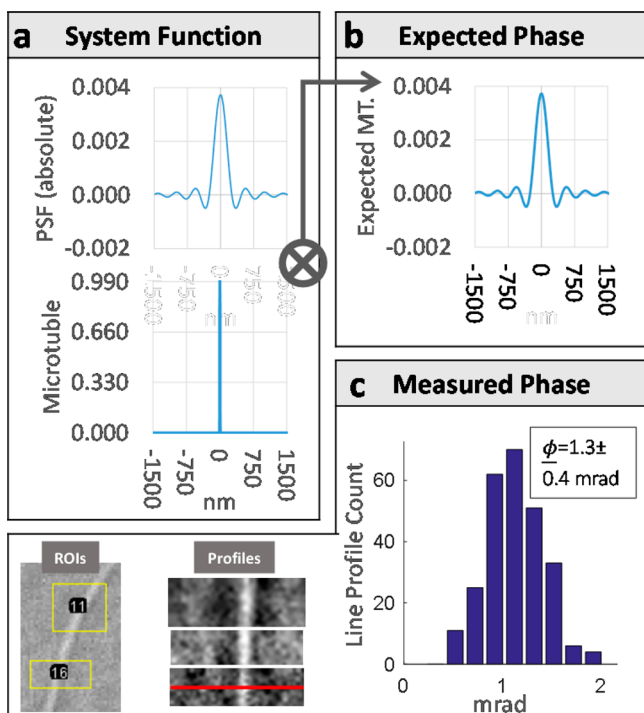
Figure 6. System response is removed to obtain the true refractive index of gliding microtubules. The diffraction limit (a) results in wide point spread function that is expected to reduce the measured phase by a factor of 15, compared to the ideal phase (b). The experimentally measured phase is computed by choosing regions of interest (ROIs) in ImageJ and rotating them so that line profiles can be drawn (c, red line). The mean of the microtubule maximum heights was found to be approximately 1.3 mrad, corresponding to a refractive index of 1.48.

in ref 35 to reduce light loss by replacing the beam splitter with custom-built optics (CellVista Pro, Phi Optics, Inc., L3 and L4 in Figure 1 are custom). Here a polarizer is used to linearize the light (P), which is then modulated by a phase-only reflection SLM. These four recorded images represent four equations with four unknowns, which are solved to obtain the phase difference between the transmitted and scattered fields (ϕ_{ac}). As outlined in ref 49, they can be further distilled to obtain the phase associated with the object (ϕ), with the reconstructed image displayed in real-time.[50]

For this experiment, the SLIM module was coupled to a Zeiss Observer Z1. All imaging was conducted with a 63× oil immersion objective (NA = 1.4, PN 420781-9910 PC3). To enable faster acquisition at maximal fields of view, we choose a sCMOS camera (Zyla 5.5, 1.4 eV readout with air-cooling), along with a high-speed SLM (Meadowlark, XY 512 series). The central wavelength was observed to be at 590 nm (HLX 64625, NAED 54248 stock halogen lamp) and is approximately colocated with the peak of the camera's quantum efficiency curve.

Sample Preparation and Experimental Protocol. SLIM images used in the gliding assay were acquired at 6.25 frames per second with 10 and 30 ms used for SLM stabilization and exposure, respectively. Although in principle, microtubules are visible at higher frame rates, such as in the 16 frames per second live video stream used to locate and focus the sample. In addition to an signal-to-noise concerns, for reasons discussed in ref 30, total acquisition was limited to conserve hard disk space.

The microtuble sample preperation protocol was inspired by ref 51. In brief, microtubules were polymerized by adding 2 mM of guanosine triphosphate (GTP) to 0.6 mg of bovine tubulin (HTS02-A, Cytoskeleton Inc.), 1:8 ratio of porcine tubulin (T240-A, Cytoskeleton Inc.) to porcine biotin-tubulin (T333P-A, Cytoskeleton Inc.) mixture (1 biotin-tubublin for every 8 tubulin), or 1:8:25 ratio of porcine

tubulin to porcine biotin-tubulin to porcine Hilyte488 labeled tubulin (RL-488M-A, Cytoskeleton Inc.). All tubulin mixtures were dissolved in BRB80 buffer (80 mM piperazine-N,N'-bis(2-ethanesulfonic acid) (PIPES), 1 mM MgCl$_2$, 1 mM ethylene glycol-bis(β-aminoethyl ether)-N,N,N',N'-tetraacetic acid (EGTA), pH 6.8). The sample was then incubated at 37 °C for 30 min. Microtubule stabilizing agent (0.05 mM paclitaxel, TXD01, Cytoskeleton Inc.) was then added to the sample with BRB80 buffer, and the sample was centrifuged at 15,000 g for 30 min to remove unpolymerized tubulin. The microtubule is stored in 0.05 mM paclitaxel solution with 1 mM GTP before the experiment.

For the microtubule gliding assay, the coverslip was coated with 5% biotin-PEG and PEG (biotin-poly ethylene glycol). Streptavidin in the concentration of 10 mg/mL was diluted in BRB80-BSA (80 mM PIPES, 1 mM MgCl$_2$, 1 mM EGTA, 8 mg/mL bovine serum albumin (BSA) pH 6.8) 10× and added to the PEG-Biotin (PEG-biotin) channel. Approximately, 0.1 μM C-terminus biotinylated-K432 kinesin-1 was used to bind to the streptavidin diluted in BRB80-BSA. Thereafter, the chamber was washed with BRB80-BSA plus 0.2 mM of free biotin to saturate the unbound streptavidin on the surface. Imaging buffer was prepared by 90 μL BRB80-BSA, 1 μL paclitaxel, 1 μL protocatechuate 3,4-dioxygen (PCD) (oxygen scavenging enzyme), 2 μL protocatechuate acid (PCA) (substrate for PCD), and 0.2 μL THP (reducing agent, 71194, EMD Millipore). Next, previously prepared microtubules were diluted at 50× and flowed into the sample chamber with 2 mM of (final) ATP concentration.

Tracking Microtubules. Manual tracking was performed using the MTrackJ plugin for Fiji.[52,53] As all microtubules were moving, we tracked all sizes. Figure 4 summarizes the primary outcome of this procedure. Specifically, we applied a cumulative moving average combined with a slight spatial high-pass before manual segmentation.[54] In this case, the ith frame in the time lapse, is updated according to the recurrence formula:

$$f(x, y) = 0.1f(x, y)_i + 0.9f(x, y)_{i-1} \qquad (2)$$

Although experiments were conducted with the raw SLIM image, owing to the simplicity of the schemes outlined above, the filtering method is now implemented in real-time. In the "live mode", used to setup the experiment, a rolling average is substituted with a five tap median filter implemented as a per-pixel sorting network.[55]

Phase Shift from a Single Microtubule. In order to describe the measured SLIM signal from a single microtubule, we start with the inhomogeneous Helmholtz equation:

$$\nabla^2 U(\mathbf{r}, \omega) + n_o^2 \beta_o^2 U(\mathbf{r}, \omega) = -\beta_o^2 \chi(\mathbf{r}) U(\mathbf{r}, \omega) \qquad (3)$$

In eq 3, U is the scalar optical field with the sum between the incident and scattered fields, $U = U_0 + U_1$, $\mathbf{r}$ is the spatial coordinate, ω the angular (temporal) frequency, n_o is the refractive index of the surrounding medium, χ is the scattering potential associated with a microtubule $\chi(\mathbf{r}) = n^2 - n_o^2$ with a refractive index of n^2.

Because of their dimensions, scattering by microtubules can be well described by the first-order Born approximation. Thus, on the right-hand side, we replace the total field with the incident one, indicating that the scattered field, U_1, is only a small perturbation to the incident field U_0. Thus, eq 3 can be split into a homogeneous and inhomogeneous portion, governing the incident and scattered fields, respectively:

$$\nabla^2 U_0(\mathbf{r}, \omega) + n_o^2 \beta_o^2 U_0(\mathbf{r}, \omega) = 0 \qquad (4a)$$

$$\nabla^2 U_1(\mathbf{r}, \omega) + n_o^2 \beta_o^2 U_1(\mathbf{r}, \omega) = -\beta_o^2 \chi(\mathbf{r}) U_0(\mathbf{r}, \omega) \qquad (4b)$$

Taking the 3D Fourier transform with respect to $\mathbf{r}$, eq 4b yields the solution for the scattered field, right away:

$$U_1(\mathbf{k}, \omega) = -\frac{\beta_o^2 \chi(\mathbf{k}) \otimes U_0(\mathbf{k})}{\beta_o^2 - \mathbf{k}^2} \qquad (5)$$

$$U_1(\mathbf{k}, \omega) = -\frac{\beta_o^2}{2q_z}\chi(\mathbf{k})\odot U_0(\mathbf{k})\left[\frac{1}{q_z - k_z} + \frac{1}{q_z + k_z}\right]$$

In eq 5, $\odot$ stands for the convolution in the 3D $\overline{k}$-space, where $\mathbf{k} = (\mathbf{k}_\perp, k_z)$ is the wavevector, and $q_z = \sqrt{\beta_o^2 - k_\perp^2}$, with $k_\perp = |\mathbf{k}_\perp|$.

Since SLIM measurements are performed in transmission, we neglect the $1/(q_z + k_z)$ in eq 5. For a plane wave incident field along z, $U_0(\mathbf{r},\omega) = A(\omega)e^{i\beta_o z}$, $U_0(\mathbf{k};\omega) = A(\omega)\cdot\delta(\mathbf{k} - \beta_o\hat{z})$, eq 5 becomes

$$U_1(\mathbf{k}, \omega) = -A(\omega)\frac{\beta_o^2}{2q_z}\frac{\chi(\mathbf{k} - \beta_o\hat{z})}{q_z - k_z} \tag{6}$$

Taking the inverse Fourier transform of eq 6, with respect to k_z, we obtain the scattered field along the spatial axis. In order to calculate this, note the following pairs of Fourier transforms with respect to the z-axis:

$$\chi(\mathbf{k} - \beta_o\hat{z}) \leftrightarrow \chi(\mathbf{k}_\perp, z)e^{i\beta_o z} \tag{7a}$$

$$\frac{1}{q_z - k_z} \leftrightarrow i\frac{e^{iq_z z}}{q_z}, \quad z \geq 0 \tag{7b}$$

where $\leftrightarrow$ denotes a Fourier pair. Combining these results, we obtain the following expression for the scattered field:

$$U_1(\mathbf{k}_\perp, z; \omega) = -i\beta_o^2 A(\omega)\frac{e^{iq_z z}}{2q_z}\cdot\chi(\mathbf{k}_\perp, q_z - \beta_o) \tag{8}$$

The total field after the object is

$$U(\mathbf{k}_\perp, z; \omega) = U_0(\mathbf{k}_\perp, z; \omega) + U_1(\mathbf{k}_\perp, z; \omega)$$
$$= A(\omega)\delta(\mathbf{k}_\perp)e^{i\beta_o z} - i\beta_o^2 A(\omega)\frac{e^{iq_z z}}{2q_z}\cdot\chi(\mathbf{k}_\perp, q_z - \beta) \tag{9}$$

Since the microtubule is much thinner than the depth of field of the imaging system, there is no optical sectioning effect, and we can assume $q_z = \sqrt{\beta_o^2 - \mathbf{k}_\perp^2} \simeq \beta_o$. Using the central ordinate theorem, we can establish that for such a thin object, the refractive index information is integrated in z, namely, $\chi(\mathbf{k}_\perp, q_z - \beta) = \int_{-\Delta/2}^{\Delta/2}\chi(\mathbf{k}_\perp, z) dz$, where Δ is the diameter of the tube. As a result, the total field can be written as

$$U(\mathbf{k}_\perp, z; \omega) = A(\omega)\delta(\mathbf{k}_\perp)e^{i\beta_o z} - i\frac{\beta_o A(\omega)}{2}e^{i\beta_o z}\Delta[n^2(\mathbf{k}_\perp) - n_o^2] \tag{10}$$

The field is measured at the image plane, which can now be easily obtained by Fourier transforming eq 10 with respect to $\mathbf{k}_\perp$:

$$U(\mathbf{r}; \omega) = A(\omega)e^{i\beta_o z}\left[1 - i\frac{\beta_o\Delta}{2}[n^2(x, y) - n_o^2]\right]$$
$$= A(\omega)e^{i\beta_o z}[1 - i\beta_o\Delta n_o[n - n_o]] \simeq A(\omega)e^{i[\beta_o z - n_o\beta_o\Delta[n - n_o]]} \tag{11}$$

Clearly, for such a thin object, QPI is expected to produce measurements of phase that are linear with the microtubule diameter and refractive index:

$$\phi(x, y) = n_o\beta_o\Delta[n(x, y) - n_o] \tag{12}$$

The diffraction limited resolution can be accounted for by convolving the total field by a point spread function (PSF) $h(x,y)$:

$$\underline{U}(\mathbf{r}, \omega) \propto e^{i\phi(x,y)}\odot h(x, y) \tag{13}$$

For small phase shifts, eq 13 yields an approximate relation, directly in phase:

$$\underline{\phi}(\mathbf{r}, \omega) \propto \phi(x, y)\odot h(x, y) \tag{14}$$

where $\underline{\phi}$ represents the measured phase, which is expected to be different from the phase shift ϕ, as result of the resolution limit. As shown in Figure 6a, for isolated objects much smaller than the resolution limit of the system, the field at the detector is dominated by the influence of the PSF. For a NA = 1.4 objective, the ratio of the peak phase value thus becomes $\underline{\phi}/\phi \approx 0.065$. Note that the PSF not only blurs the image but also is expected to reduce the measured phase value by ~15 times (Figure 6b). This knowledge can then be used to obtain a refined measure for the true refractive index of the microtubule:

$$n_{\text{microtuble}} = n_o + \underline{\phi}\frac{\lambda}{2\pi h} \tag{15}$$

As shown in Figure 6c, the experimentally measured refractive index is 1.475 at 590 nm.

ASSOCIATED CONTENT

$\mathbf{S}$ Supporting Information

is provided as Supporting Information. The image sequences shown in Figures 1 and 3 can be found on the publisher's Web site (in movie form). The Supporting Information is available free of charge on the ACS Publications website at DOI: 10.1021/acsnano.6b06945.

A derivation of the full-field light scattering technique used in Figure 5 (PDF)

Video 1: Portion of a typical phase contrast image sequence, shown in Figure 1a (AVI)

Video 2: Portion of a typical SLIM image sequence (no-enhancement), shown in Figure 2b (AVI)

Video 3: Portion of an epifluorescence image sequence, shown in Figure 3a (AVI)

Video 4: Portion of a SLIM image sequence (no-enhancement), shown in Figure 3b (AVI)

Video 5: Portion of a SLIM image sequence (digitally enhanced) shown in Figure 3c (AVI)

AUTHOR INFORMATION

Corresponding Author

*E-mail: gpopescu@illinois.edu.

ORCID

Mikhail E. Kandel: 0000-0003-2124-7750

Notes

The authors declare the following competing financial interest(s): G.P. has financial interest in Phi Optics, Inc., a company that commercializes quantitative phase imaging systems.

REFERENCES

(1) Kirschner, M.; Mitchison, T. Beyond Self-Assembly: From Microtubules to Morphogenesis. *Cell* **1986**, *45*, 329−342.

(2) Akhmanova, A.; Dogterom, M. Kinesins Lead Aging Microtubules to Catastrophe. *Cell* **2011**, *147*, 966−968.

(3) Brugues, J.; Nuzzo, V.; Mazur, E.; Needleman, D. J. Nucleation and Transport Organize Microtubules in Metaphase Spindles. *Cell* **2012**, *149*, 554−564.

(4) Schaletzky, J.; Rape, M. Getting a Grip on Microtubules. *Cell* **2016**, *164*, 836−837.

(5) Vicsek, T. Biological Physics: Swarming Microtubules. *Nature* **2012**, *483*, 411−412.

(6) Small, J. V.; Geiger, B.; Kaverina, I.; Bershadsky, A. How Do Microtubules Guide Migrating Cells? *Nat. Rev. Mol. Cell Biol.* **2002**, *3*, 957−964.

(7) de Pablo, P. J.; Schaap, I. A.; MacKintosh, F. C.; Schmidt, C. F. Deformation and Collapse of Microtubules on the Nanometer Scale. *Phys. Rev. Lett.* **2003**, *91*, 098101.

(8) Kadavath, H.; Hofele, R. V.; Biernat, J.; Kumar, S.; Tepper, K.; Urlaub, H.; Mandelkow, E.; Zweckstetter, M. Tau Stabilizes Microtubules by Binding at the Interface between Tubulin Heterodimers. *Proc. Natl. Acad. Sci. U. S. A.* **2015**, *112*, 7501−7506.

(9) Mohan, R.; Katrukha, E. A.; Doodhi, H.; Smal, I.; Meijering, E.; Kapitein, L. C.; Steinmetz, M. O.; Akhmanova, A. End-Binding Proteins Sensitize Microtubules to the Action of Microtubule-Targeting Agents. *Proc. Natl. Acad. Sci. U. S. A.* **2013**, *110*, 8900−8905.

(10) Vale, R. D. The Molecular Motor Toolbox for Intracellular Transport. *Cell* **2003**, *112*, 467−480.

(11) Kulic, I. M.; Brown, A. E.; Kim, H.; Kural, C.; Blehm, B.; Selvin, P. R.; Nelson, P. C.; Gelfand, V. I. The Role of Microtubule Movement in Bidirectional Organelle Transport. *Proc. Natl. Acad. Sci. U. S. A.* **2008**, *105*, 10011−10016.

(12) Okada, N.; Sato, M. Spatiotemporal Regulation of Nuclear Transport Machinery and Microtubule Organization. *Cells* **2015**, *4*, 406−426.

(13) Barisic, M.; Silva e Sousa, R.; Tripathy, S. K.; Magiera, M. M.; Zaytsev, A. V.; Pereira, A. L.; Janke, C.; Grishchuk, E. L.; Maiato, H. Mitosis. Microtubule Detyrosination Guides Chromosomes During Mitosis. *Science* **2015**, *348*, 799−803.

(14) Jordan, M. A.; Wilson, L. Microtubules and Actin Filaments: Dynamic Targets for Cancer Chemotherapy. *Curr. Opin. Cell Biol.* **1998**, *10*, 123−130.

(15) Goedert, M.; Spillantini, M. G.; Jakes, R.; Rutherford, D.; Crowther, R. A. Multiple Isoforms of Human Microtubule-Associated Protein Tau: Sequences and Localization in Neurofibrillary Tangles of Alzheimer's Disease. *Neuron* **1989**, *3*, 519−526.

(16) Bermudes, D.; Hinkle, G.; Margulis, L. Do Prokaryotes Contain Microtubules? *Microbiol Rev.* **1994**, *58*, 387−400.

(17) Heggeness, M. H.; Simon, M.; Singer, S. J. Association of Mitochondria with Microtubules in Cultured Cells. *Proc. Natl. Acad. Sci. U. S. A.* **1978**, *75*, 3863−3866.

(18) Brangwynne, C. P.; Koenderink, G. H.; Mackintosh, F. C.; Weitz, D. A. Nonequilibrium Microtubule Fluctuations in a Model Cytoskeleton. *Phys. Rev. Lett.* **2008**, *100*, 118104.

(19) Chung, P. J.; Choi, M. C.; Miller, H. P.; Feinstein, H. E.; Raviv, U.; Li, Y.; Wilson, L.; Feinstein, S. C.; Safinya, C. R. Direct Force Measurements Reveal That Protein Tau Confers Short-Range Attractions and Isoform-Dependent Steric Stabilization to Microtubules. *Proc. Natl. Acad. Sci. U. S. A.* **2015**, *112*, E6416−6425.

(20) Na, S.; Collin, O.; Chowdhury, F.; Tay, B.; Ouyang, M.; Wang, Y.; Wang, N. Rapid Signal Transduction in Living Cells Is a Unique Feature of Mechanotransduction. *Proc. Natl. Acad. Sci. U. S. A.* **2008**, *105*, 6626−6631.

(21) Zhang, J.; Guo, W. H.; Wang, Y. L. Microtubules Stabilize Cell Polarity by Localizing Rear Signals. *Proc. Natl. Acad. Sci. U. S. A.* **2014**, *111*, 16383−16388.

(22) Yildiz, A.; Tomishige, M.; Vale, R. D.; Selvin, P. R. Kinesin Walks Hand-over-Hand. *Science* **2004**, *303*, 676−678.

(23) Zhao, T.; Graham, O. S.; Raposo, A.; St. Johnston, D. Growing Microtubules Push the Oocyte Nucleus to Polarize the Drosophila Dorsal-Ventral Axis. *Science* **2012**, *336*, 999−1003.

(24) Waterman-Storer, C. M.; Salmon, E. Actomyosin-Based Retrograde Flow of Microtubules in the Lamella of Migrating Epithelial Cells Influences Microtubule Dynamic Instability and Turnover and Is Associated with Microtubule Breakage and Treadmilling. *J. Cell Biol.* **1997**, *139*, 417−434.

(25) Waterman-Storer, C. M.; Salmon, E. D. How Microtubules Get Fluorescent Speckles. *Biophys. J.* **1998**, *75*, 2059−2069.

(26) Editorial, Artifacts of Light. *Nat. Methods* **2013**, *10*, 1135−1135.10.1038/nmeth.2760

(27) Hoebe, R. A.; Van Oven, C. H.; Gadella, T. W., Jr.; Dhonukshe, P. B.; Van Noorden, C. J.; Manders, E. M. Controlled Light-Exposure Microscopy Reduces Photobleaching and Phototoxicity in Fluorescence Live-Cell Imaging. *Nat. Biotechnol.* **2007**, *25*, 249−253.

(28) Inoue, S.; Fuseler, J.; Salmon, E. D.; Ellis, G. W. Functional Organization of Mitotic Microtubules - Physical-Chemistry of Invivo Equilibrium System. *Biophys. J.* **1975**, *15*, 725−744.

(29) Svoboda, K.; Schmidt, C. F.; Schnapp, B. J.; Block, S. M. Direct Observation of Kinesin Stepping by Optical Trapping Interferometry. *Nature* **1993**, *365*, 721−727.

(30) Andrecka, J.; Ortega Arroyo, J.; Lewis, K.; Cross, R. A.; Kukura, P. Label-Free Imaging of Microtubules with Sub-Nm Precision Using Interferometric Scattering Microscopy. *Biophys. J.* **2016**, *110*, 214−217.

(31) Ortega-Arroyo, J.; Kukura, P. Interferometric Scattering Microscopy (Iscat): New Frontiers in Ultrafast and Ultrasensitive Optical Microscopy. *Phys. Chem. Chem. Phys.* **2012**, *14*, 15625−15636.

(32) Zilker, A.; Engelhardt, H.; Sackmann, E. Dynamic Reflection Interference Contrast (Ric-) Microscopy - a New Method to Study Surface Excitations of Cells and to Measure Membrane Bending Elastic-Moduli. *J. Phys.* **1987**, *48*, 2139−2151.

(33) Kim, T.; Zhou, R. J.; Mir, M.; Babacan, S. D.; Carney, P. S.; Goddard, L. L.; Popescu, G. White-Light Diffraction Tomography of Unlabelled Live Cells. *Nat. Photonics* **2014**, *8*, 256−263.

(34) Wang, Z.; Marks, D. L.; Carney, P. S.; Millet, L. J.; Gillette, M. U.; Mihi, A.; Braun, P. V.; Shen, Z.; Prasanth, S. G.; Popescu, G. Spatial Light Interference Tomography (Slit). *Opt. Express* **2011**, *19*, 19907−19918.

(35) Wang, Z.; Millet, L.; Mir, M.; Ding, H.; Unarunotai, S.; Rogers, J.; Gillette, M. U.; Popescu, G. Spatial Light Interference Microscopy (Slim). *Opt. Express* **2011**, *19*, 1016−1026.

(36) Popescu, G. *Quantitative Phase Imaging of Cells and Tissues*; McGraw-Hill: New York, 2011; p 385.

(37) Gabor, D. A New Microscopic Principle. *Nature* **1948**, *161*, 777.

(38) Wang, Z.; Popescu, G. Quantitative Phase Imaging with Broadband Fields. *Appl. Phys. Lett.* **2010**, *96*, 051117.

(39) Reed, N. A.; Cai, D.; Blasius, T. L.; Jih, G. T.; Meyhofer, E.; Gaertig, J.; Verhey, K. J. Microtubule Acetylation Promotes Kinesin-1 Binding and Transport. *Curr. Biol.* **2006**, *16*, 2166−2172.

(40) Vale, R. D.; Malik, F.; Brown, D. Directional Instability of Microtubule Transport in the Presence of Kinesin and Dynein, Two Opposite Polarity Motor Proteins. *J. Cell Biol.* **1992**, *119*, 1589−1596.

(41) LaPointe, N. E.; Morfini, G.; Brady, S. T.; Feinstein, S. C.; Wilson, L.; Jordan, M. A. Effects of Eribulin, Vincristine, Paclitaxel and Ixabepilone on Fast Axonal Transport and Kinesin-1 Driven Microtubule Gliding: Implications for Chemotherapy-Induced Peripheral Neuropathy. *NeuroToxicology* **2013**, *37*, 231−239.

(42) Minoura, I.; Hachikubo, Y.; Yamakita, Y.; Takazaki, H.; Ayukawa, R.; Uchimura, S.; Muto, E. Overexpression, Purification, and Functional Analysis of Recombinant Human Tubulin Dimer. *FEBS Lett.* **2013**, *587*, 3450−3455.

(43) Mann, H. B.; Whitney, D. R. On a Test of Whether One of Two Random Variables Is Stochastically Larger Than the Other. *Ann. Math. Stat.* **1947**, *18*, 50−60.

(44) Wang, R.; Wang, Z.; Millet, L.; Gillette, M. U.; Levine, A. J.; Popescu, G. Dispersion-Relation Phase Spectroscopy of Intracellular Transport. *Opt. Express* **2011**, *19*, 20571−20579.

(45) Wang, R.; Lei, L.; Wang, Y.; Levine, A. J.; Popescu, G. Dispersion-Relation Fluorescence Spectroscopy. *Phys. Rev. Lett.* **2012**, *109*, 188104.

(46) Ding, H.; Wang, Z.; Nguyen, F.; Boppart, S. A.; Popescu, G. Fourier Transform Light Scattering of Inhomogeneous and Dynamic Structures. *Phys. Rev. Lett.* **2008**, *101*, 238102.

(47) Schnitzer, M. J.; Block, S. M. Kinesin Hydrolyses One Atp Per 8-Nm Step. *Nature* **1997**, *388*, 386−390.

(48) Bohm, K. J.; Stracke, R.; Baum, M.; Zieren, M.; Unger, E. Effect of Temperature on Kinesin-Driven Microtubule Gliding and Kinesin Atpase Activity. *FEBS Lett.* **2000**, *466*, 59−62.

(49) Bhaduri, B.; Tangella, K.; Popescu, G. Fourier Phase Microscopy with White Light. *Biomed. Opt. Express* **2013**, *4*, 1434−1441.

(50) Kandel, M. E.; Luo, Z.; Han, K.; Popescu, G. C++ Software Integration for a High-Throughput Phase Imaging Platform. *Proc. SPIE* **2015**, *9336*, 93360Z.

(51) Case, R. B.; Pierce, D. W.; HomBooher, N.; Hart, C. L.; Vale, R. D. The Directional Preference of Kinesin Motors Is Specified by an Element Outside of the Motor Catalytic Domain. *Cell* **1997**, *90*, 959−966.

(52) Meijering, E.; Dzyubachyk, O.; Smal, I. Methods for Cell and Particle Tracking. In *Methods in Enzymology*; Conn, P. M., Ed.; Academic Press: San Diego, CA, 2012; Vol. *504*, pp 183−200.

(53) Schindelin, J.; Arganda-Carreras, I.; Frise, E.; Kaynig, V.; Longair, M.; Pietzsch, T.; Preibisch, S.; Rueden, C.; Saalfeld, S.; Schmid, B.; Tinevez, J. Y.; White, D. J.; Hartenstein, V.; Eliceiri, K.; Tomancak, P.; Cardona, A. Fiji: An Open-Source Platform for Biological-Image Analysis. *Nat. Methods* **2012**, *9*, 676−682.

(54) Walter, J. *FFT Filter*. http://rsb.info.nih.gov/ij/plugins/fft-filter.html (accessed December 4, 2016).

(55) Lewis, F. D. *Sorting Networks*. http://cs.engr.uky.edu/~lewis/essays/algorithms/sortnets/sort-net.html (accessed December 4, 2016).